RECENT OBSERVATIONS OF DEEP CONVECTION: TOGA COARE

R H Johnson
Colorado State University
Fort Collins, Colorado, USA

Summary: This paper is a highly abbreviated review of convection during TOGA COARE. Convection was modulated on a wide range of time (and space) scales, all the way from the 30-60 intraseasonal oscillations down to the diurnal and subdiurnal time scales of individual convective systems. Deep convection produced most of the rainfall in COARE, but shallower convective cells involving the warm-rain process were also prevalent. The diurnal cycle was complex: large convective systems exhibited a nighttime maximum, while smaller systems frequently peaked in early afternoon and evening in response to ocean surface heating. Strong feedbacks between the ocean and atmospheric convection existed throughout the experiment

1. INTRODUCTION

Tropical field experiments in the last several decades such as GATE, MONEX, AMEX, etc., have provided an enhanced understanding of the spectrum of convective phenomena, the cloud and precipitation structure of convective systems, internal circulations within convection, and the relationship of convective structures to the environmental flow. However, a number of important questions remain: What determines the organizational characteristics of convective systems? How do these characteristics influence surface fluxes and momentum transport? What controls the diurnal cycle of convection? What is the nature of the coupling between convection and the upper ocean? All of these questions have an important bearing on numerical weather prediction and the parameterization of convection in prediction models. The recent Tropical-Ocean Global-Atmosphere Coupled Ocean-Atmosphere Response Experiment (TOGA COARE) of November 1992 – February 1993 (Webster and Lukas 1992) has provided an unprecedented data set for examining a number of these issues, particularly those related to atmosphere-ocean coupling. This paper will deal principally with recent results from TOGA COARE, although due of limited space, many observations (e.g., from aircraft and ships) will not be treated.

2. BROADSCALE CONSIDERATIONS

The four-month Intensive Observing Period (IOP) of COARE occurred near the onset of a weak-ENSO event. SST and Outgoing Longwave Radiation (OLR) anomalies for three of the four months (Fig. 1, from Gutzler et al. 1994) show positive SST anomalies and enhanced cloudiness near the date line. The IOP-mean brightness temperatures (Fig. 2a, from Lin and Johnson 1996a) indicate that the maximum deep convection occurred east of the Intensive Flux Array (IFA; polygon between 150 and

160°E) with the suggestion of a double-ITCZ structure between the IFA and the date line. However, considerable variability existed on a month-to-month basis: November and February had mean double-ITCZ structures (Figs. 2b and 2e), while December and January had single ITCZ bands (Figs. 2c and 2d).

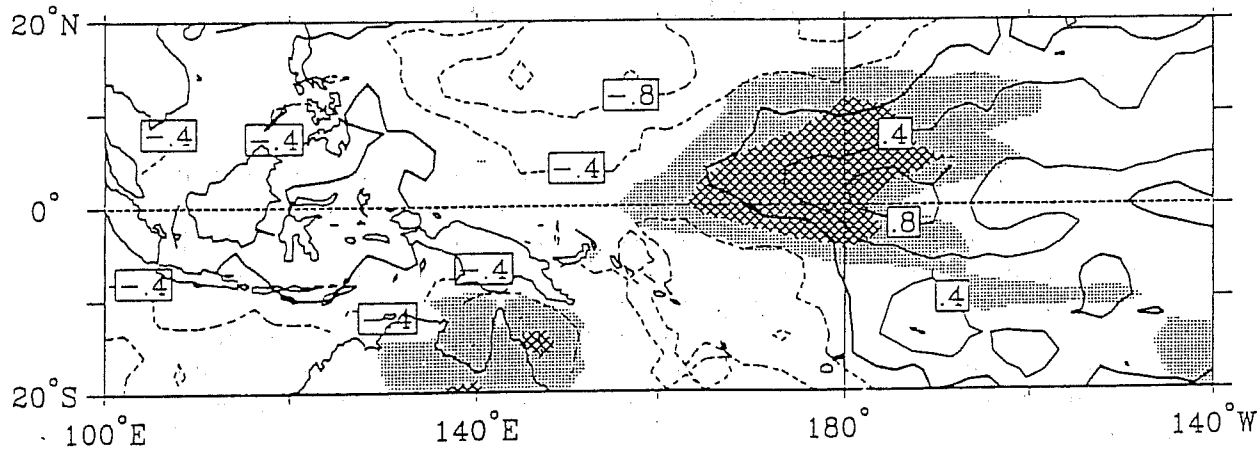

Figure 1: Three month average SSTA's for the December-February of the COARE IOP. Light shading is for OLR anomalies < - 10 W m^{-2}, hatching for OLRA's < -20 W m^{-2}. Adapted from Gutzler et al. (1994).

Convection during COARE was modulated over a wide range of time scales, all the way from the 30-60 day scale of the intraseasonal oscillation (ISO) down to bi-diurnal, diurnal and subdiurnal scales associated with individual or groups of convective systems. ISO variability can be seen in a time-longitude diagram of OLR (Fig. 3a, from Nakazawa 1995), where several ISO events are observed propagating eastward through the COARE domain. Maximum zonal winds at 850 hPa (Fig. 3b) lagged slightly behind the maximum OLR.

The phase relationship can be better seen in Fig. 4, a time series of the IFA-averaged zonal wind, precipitation (P), evaporation (E) and SST. P is determined from the moisture budget and E from the application of the COARE bulk algorithm (Fairall et al. 1996) to buoys in the IFA. Three low-level westerly wind bursts occurred, with the most prominent one peaking around January 1. Low-level westerlies and E can be seen to peak approximately one to two weeks after the maximum rainfall. Averaged over the entire IOP, $E \approx 3$ to 4 mm day^{-1} and $P \approx 6$ mm day^{-1}, i.e., P was about twice E over the IFA. However, regionally, P was a local minimum over the IFA. Considerably greater precipitation rates ($P \gg E$) were observed in east-west ITCZ bands north and south of the IFA (near 5°N and 5°S) and to the east of the IFA. During the heavy-rain periods, P exceeded E by 3 to 5 times (Fig. 4) the excess arising from large-scale moisture convergence (water vapor storage was small).

As noted by Webster (1994), Nakazawa (1995), Lin and Johnson (1996a) and Chen et al. (1996), the SST had an intraseasonal signal in lagged quadrature with the rainfall in COARE (Fig. 4). During

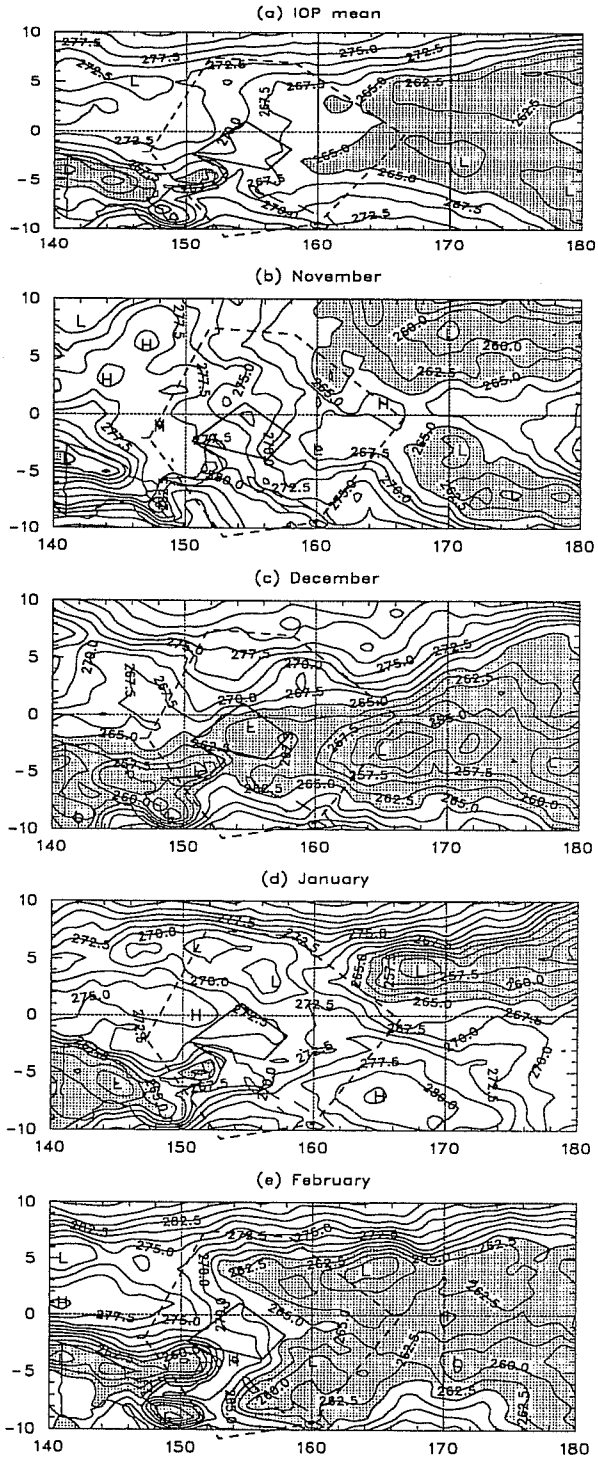

Figure 2: IOP-mean and monthly mean brightness temperatures over the large Scale Array. Areas with temperature less than 265 K are shaded. (a) IOP mean, (b) November, (c) December, (d) January, (e) February.

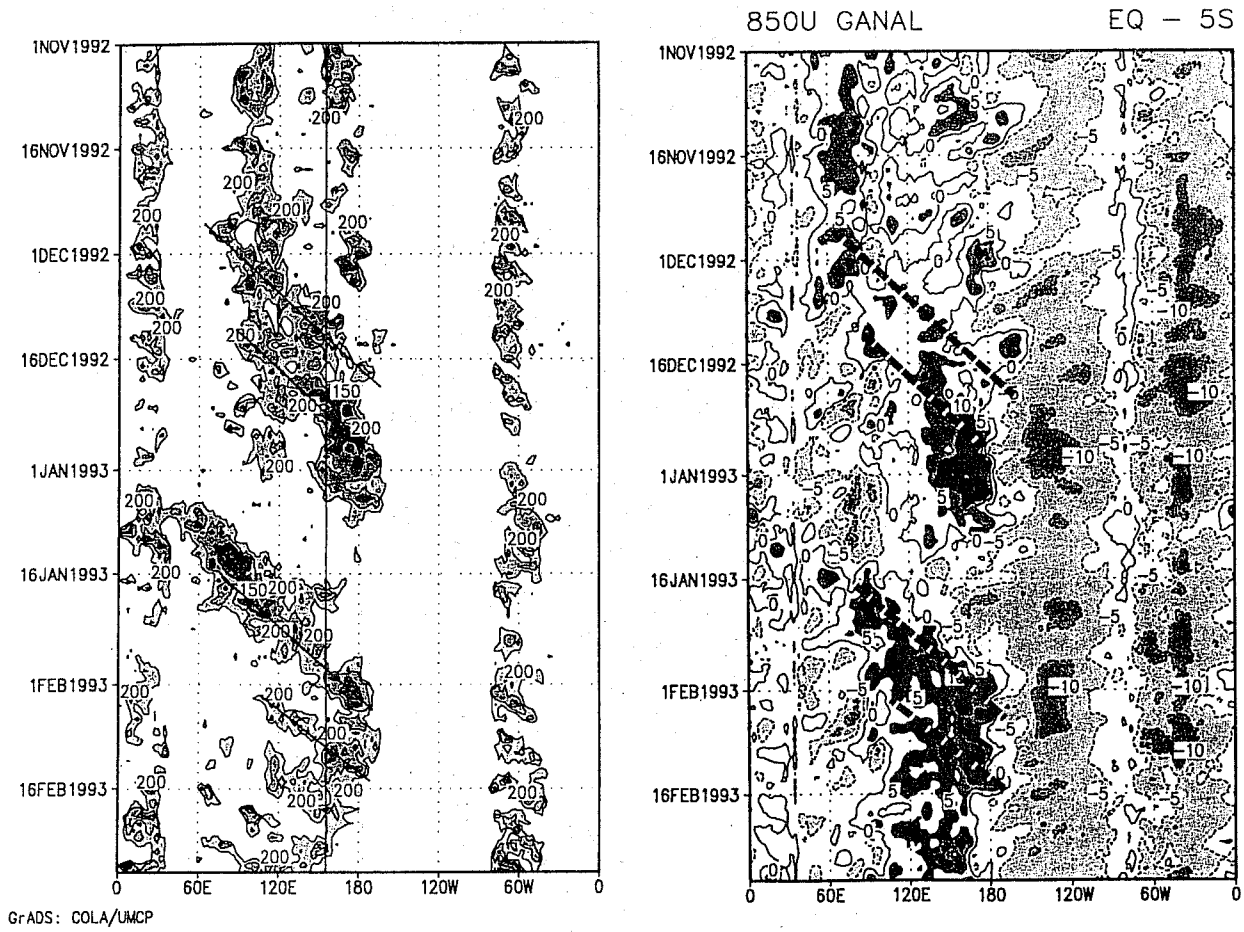

Figure 3: (Left) Outgoing Longwave Radiation (OLR) from NOAA polar orbiting satellites, averaged between the equator and 5°S during the COARE IOP. Contours drawn for OLR < 200 W m^{-2}, with contour interval of 25 W m^{-2}. Slanted lines show subjectively determined center longitudes of super clusters. (Right) Zonal winds at 850 hPa from the Japan Meteorological Agency global analysis dataset, averaged between the equator and 5°S. Light shading denotes area of less than -10 m s^{-1}, while dark shading denotes areas of more than 0 m s^{-1}. Slanted lines are from left panel. From Nakazawa (1995).

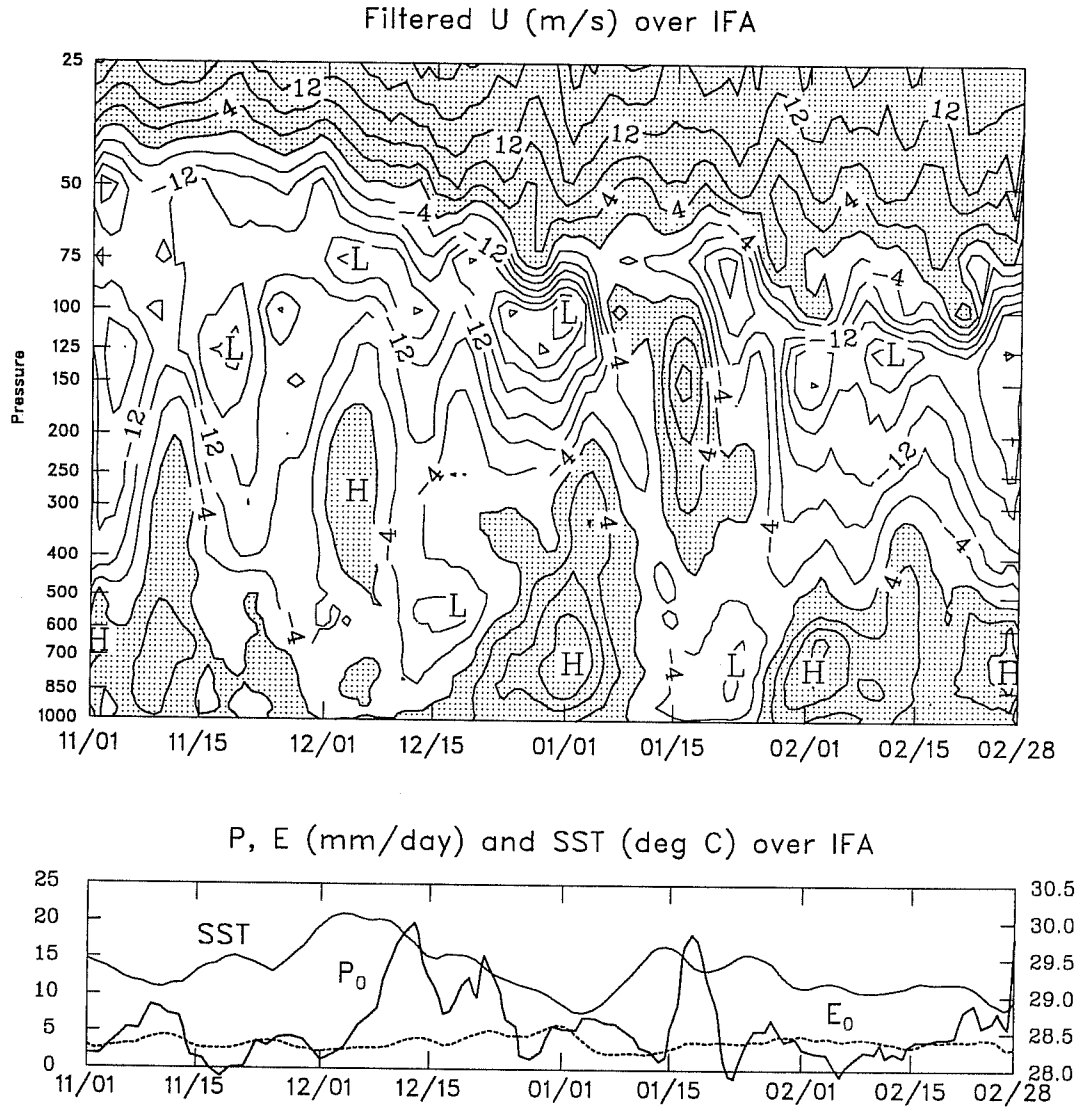

Figure 4: (Upper) Zonal component of the flow (m s^{-1}, 5-day running mean, westerlies shaded). (Lower) Precipitation (mm day^{-1}, thick solid), SST (°C, thin solid curve) and evaporation (mm day^{-1}, dotted curve) averaged over IFA.

light-wind and light-rainfall (mostly clear) periods, the SST rose, whereas during rainy and windy periods SST fell owing to enhanced evaporation, cloudiness and mixing within the upper ocean.

3. SHORT-TERM VARIABILITY

The evolution of the December westerly wind burst is illustrated in greater detail in Fig. 5 (Lin and Johnson 1996b). Beginning on about the 10th, the SST started to fall in association with increased surface winds and deep convection, as evidenced by an increase in the magnitudes of the apparent heat source Q_1 and apparent moisture sink Q_2 (as defined by Yanai et al. 1973). Several episodes of enhanced convection can be seen between the 10th and 25th, along with associated fluctuations in surface wind speed, brightness temperature and latent heat flux. Throughout the period of increasing winds, Q_1 typically peaked in the mid- to upper troposphere, whereas Q_2 peaked in the lower troposphere early on, but later in the mid- to upper troposphere. This shift represents a transition from predominantly deep convection at the start of the westerly wind burst to increasing contribution of stratiform precipitation toward the end (Q_1 and Q_2 peaks more coincident). This transition presumably occurred in response to the increasing low-level wind shear (Fig. 4), which eventually became so large by the end of the December that deep convection was cut off altogether.

The IOP-mean Q_1 and Q_2 profiles (normalized by precipitation rate following Johnson 1984) for the Outer Sounding Array (OSA; an approximate hexagon of sounding stations extending from 8°N to 10 °S) and IFA are shown in Fig. 6 (from Johnson and Lin 1996). Values for the Marshall Islands region from Yanai et al. (1973) are shown for comparison. The OSA Q_1 and Q_2 profiles resemble those for the Marshall Islands, except for the smaller amplitude of Q_2 . This difference can be explained by noting that the areas under the Q_2 curves are proportional to $1 - E/P$, which has the values 0.79 and 0.56 for the Marshall Islands and COARE OSA, respectively. In addition, both the COARE OSA and Marshall Islands Q_2 profiles show a minimum near 600 hPa or 4 km, which is associated with an inflection point in the specific humidity profile likely related in some way to the effects of melting (Johnson et al. 1996).

The Q_2 profile for the IFA, however, contrasts in several ways from those for the OSA and Marshall Islands. First, negative values can be seen below 850 hPa or 1.5 km. Second, the IFA Q_2 profile does not exhibit a prominent double-peak structure, at least for the IOP mean. There are times, however, when the IFA Q_2 profiles do resemble those for the ITCZ and Marshall Islands. An example is during a period of heavy rainfall on 11-17 December (Fig. 7), just prior to the strong westerly wind burst at the end of December (Gutzler et al. 1994, Kiladis et al. 1994). Averaged over this one-week period, Q_1 and Q_2 are positive everywhere and the peaks are displaced, indicative of deep convective activity (e.g., Yanai et al. 1973). A double peak in Q_2 is also present (though not very pronounced).

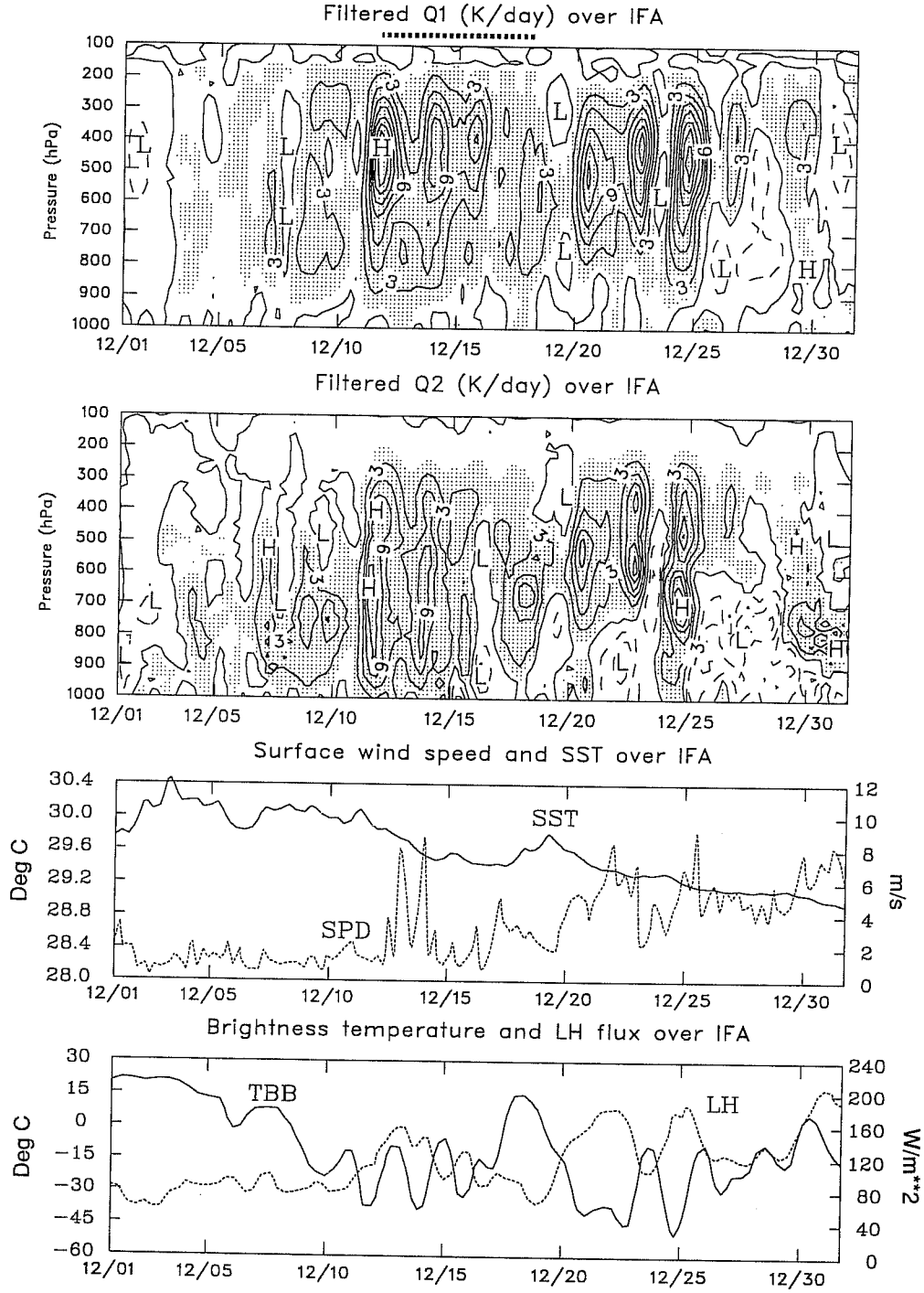

Figure 5: Monthly time series of the IFA-mean apparent heat source Q_1 (K day^{-1}), the apparent moisture source Q_2 (K day^{-1}), SST (Deg C), surface wind speed (m s^{-1}), GMS brightness temperature (Deg C) and surface latent heat flux (W m^{-2}) for December. The contour intervals for Q_1 and Q_2 are 3 K day^{-1} and areas > 1.0 K day^{-1} are shaded. Dotted lines above the Q_1 figures indicate periods during the COARE IOP when both ships *Kexue* #1 and *Shiyan* #3 were out of the IFA.

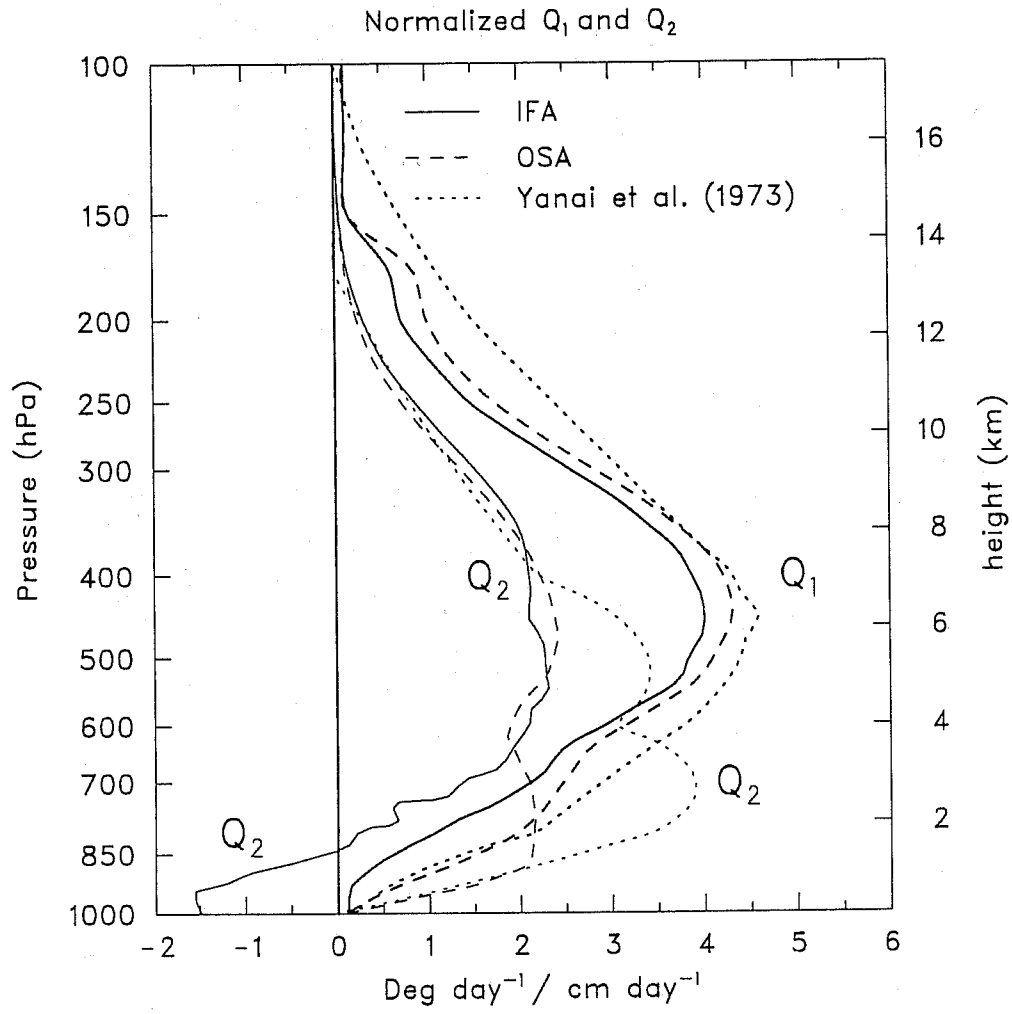

Figure 6: Profiles of Q_1 (heavy lines) and Q_2 (light lines) normalized by precipitation rate for Intensive Flux Array (IFA, solid lines), Outer sounding Array (OSA, long dashed lines)[both IOP means]and Marshall Islands (from Yanai et al. 1973, short dashed lines).

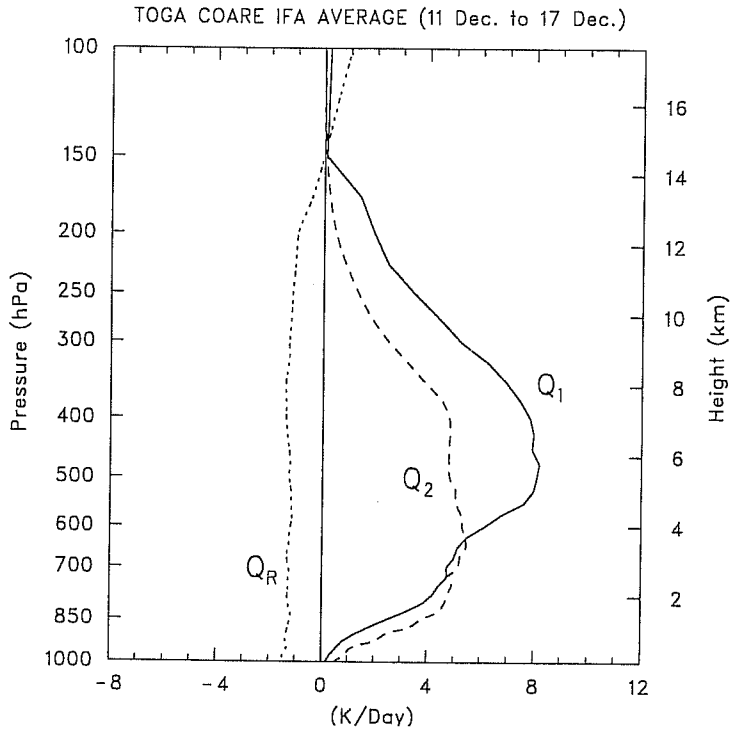

Figure 7: IFA-averaged Q_1, Q_2 and Q_R profiles for convectively disturbed period (11-17 December 1992).

To understand the causes of the low-level negative Q_2 , a time series of Q_2 for the IFA is presented (Fig. 8, Johnson and Lin 1996). Note the strong moistening below 800 hPa during the last two weeks of December and the first two weeks of February. These periods correspond to the two primary westerly wind bursts during COARE (Fig. 4). It is also evident from Fig. 4 that E is either approximately equal to or exceeds P during significant portions of these strong-wind periods. This behavior is consistent with the apparent moistening (negative Q_2) in the lowest 2-3 km in Fig. 8. This apparent moistening is accomplished by mixed-layer turbulent transport as well as transport by shallow cumulus clouds (as occurs in the Atlantic tradewind belt; Nitta and Esbensen 1974). A spectral cloud diagnostic model has been used (Johnson and Lin 1996) to determine the properties of the shallow cloud fields during the westerly wind bursts. Computed profiles of mass fluxes, entrainment, detrainment and heat and moisture balances during these periods resemble those for the western Atlantic tradewind regime. This finding leads to the conclusion that the western Pacific warm pool boundary layer develops tradewind-like characteristics with abundant shallow cumulus during westerly wind bursts and these episodic "trade-like" regimes are prominent enough to impact the seasonal distributions of boundary-layer heating and moistening.

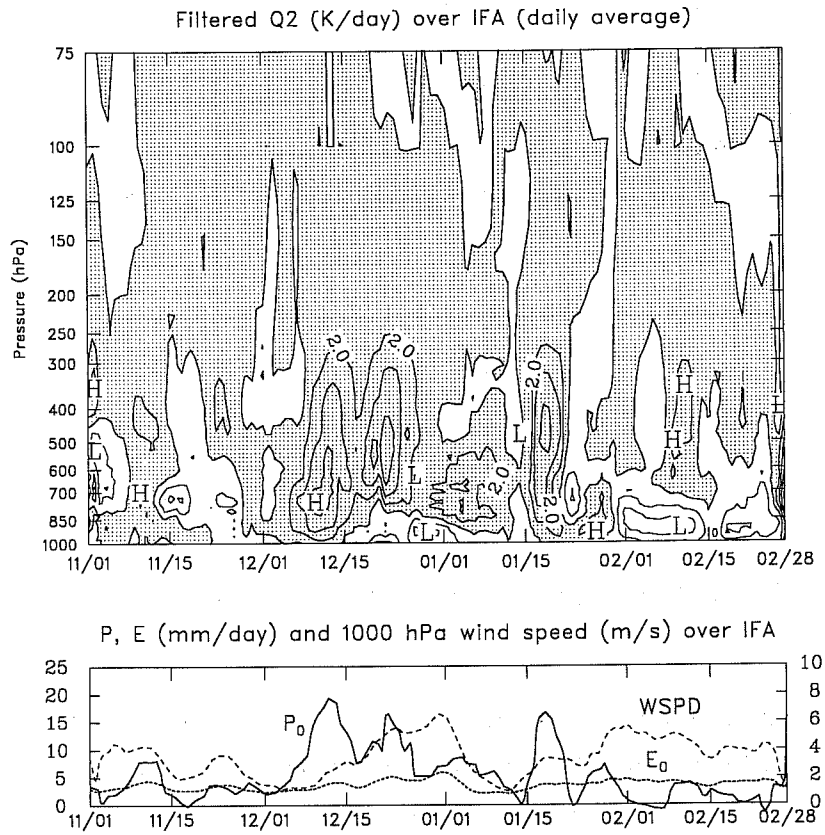

Figure 8: IOP time series (five-day running means) of Q_2 (top panel, positive values shaded) and budget-derived precipitation rate P_o and evaporation rate E_o (bottom panel) for Intensive Flux Array. Also, 1000-hPa wind speed has been added to bottom panel.

4. STRUCTURAL CHARACTERISTICS OF CONVECTION

The ship-radar program in COARE has provided a unique opportunity to determine climatological characteristics of convection over the warm pool. Using MIT radar data from the R/V *Vickers* Rickenbach and Rutledge (1996a, hereafter referred to as RR96a) have classified convection into four categories: sub-MCS linear and non-linear, and MCS linear and non-linear (Table 1). Systems are classified as MCS (mesoscale convective system) if the horizontal scale of the convection is $\geq$ 100 km.

Category	Description
Sub-MCS scale non-linear	*No linear organization, < 100 km in scale.* Population of isolated convective cells.
Sub-MCS scale linear	*Linear organization, < 100 km in scale.* Lines of convective cells, often in groups.
MCS scale non-linear	*No linear organization, ≥ 100 km in scale.* Contiguous group of convective cells, embedded in non-convective rain.
MCS scale linear	*Linear organization, ≥ 100 km in scale.* Line of convective cells with associated non-convective rain.

Table 1: Summary of the definition of each event type at the maximum level of organization: Sub-MCS scale non-linear, sub-MCS scale linear, MCS scale non-linear, and MCS scale linear. From Rickenbach and Rutledge (1996a).

A histogram of event types (Fig. 9) shows that while sub-MCS non-linear was by far the most commonly occurring mode of convection, it produced less that 15% of the rain volume. Clearly, the MCS categories produce the highest rainrates and rain volumes, with MCS-linear producing the greatest rain volume. RR96a have determined for the ninety day period of all the *Vickers'* cruises, 69% of the rainfall was convective, the remainder being stratiform or decaying convective (referred to collectively as non-convective). Broken down by event type (Table 2), sub-MCS had the largest convective rain fraction, while linear patterns within sub-MCS and MCS categories tended to yield the greatest non-convective amounts, presumably owing to the increased organized circulations within such systems.

RR96a determined the convective rain fractions for features of different heights for the four event categories (Fig. 10). For all but the sub-MCS non-linear case, the peak rainfall rate occurs for storms with tops in the upper troposphere, although a secondary maximum occurs near 9 km. The peak for the sub-MCS non-linear case is between 8 and 9 km. The latter systems typically occur in light-wind and dry mid-level air conditions, which presumably accounts for the shallower convection (weaker low-level forcing and greater dry-air entrainment). In terms of number fraction (Fig. 11), the peaks in all

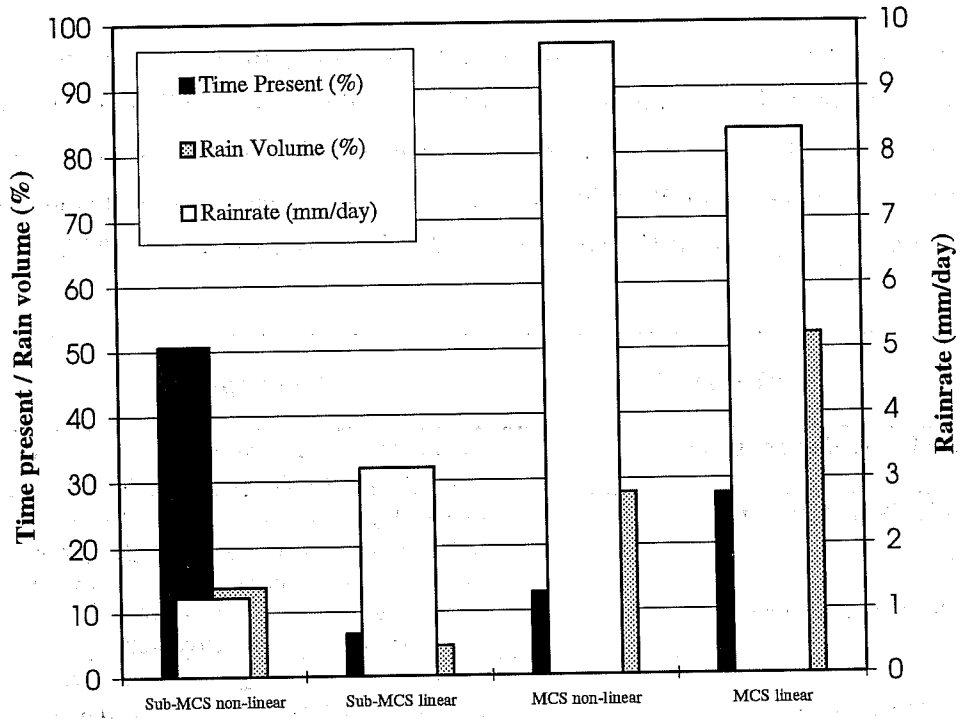

Figure 9: The time present (black), rain volume (gray), and mean rainfall rate (white, mm day^{-1}) for each event type for all three cruises combined. Time present and rain volume are expressed as fractions of the three cruise totals. From Rickenbach and Rutledge (1996a).

Category	Mean Convective Rain Fraction
Sub-MCS scale non-linear	81%
Sub-MCS scale linear	76%
MCS scale non-linear	73%
MCS scale linear	64%

Table 2: Mean convective rain fraction for each event type, averaged over all three cruises. From Rickenbach and Rutledge (1996a).

categories are between 6 and 8 km: the fewer taller cells that do occur produce the greatest rainfall amounts.

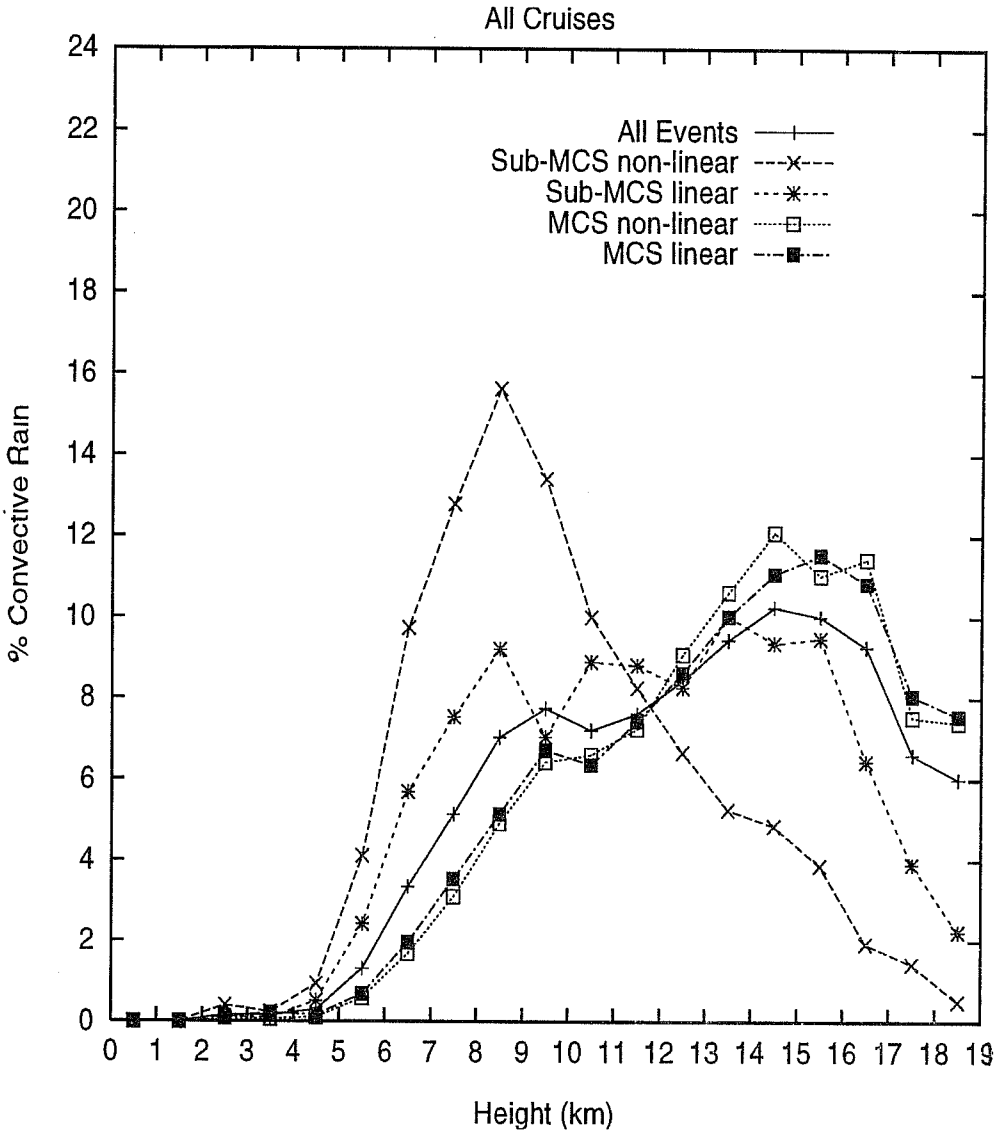

Figure 10: Histograms of the fraction of convective rain produced by convective features of various heights (1 km bins), for each event type and for all events combined. Each histogram represents the fraction of convective rain produced by that event type. Convective feature height represent the maximum height attained by the feature. From Rickenbach and Rutledge (1996a).

The large number fraction of convective events topping out between 6 and 8 km (Fig. 11) may be related to the commonly occurring stable layers near the 0°C level over the warm pool (Johnson et al. 1996, Mapes and Zuidema 1996). Figure 12 shows a time series of the temperature lapse rate over the IFA (computed from 25-hPa resolution data) for the four-month IOP (from Johnson et al. 1996). Notice the frequent increased stability just below 6 km near the 0°C level, as well as near the trade-inversion level or 2 km. The 0°C stable layers may retard the growth of entraining, precipitation-laden

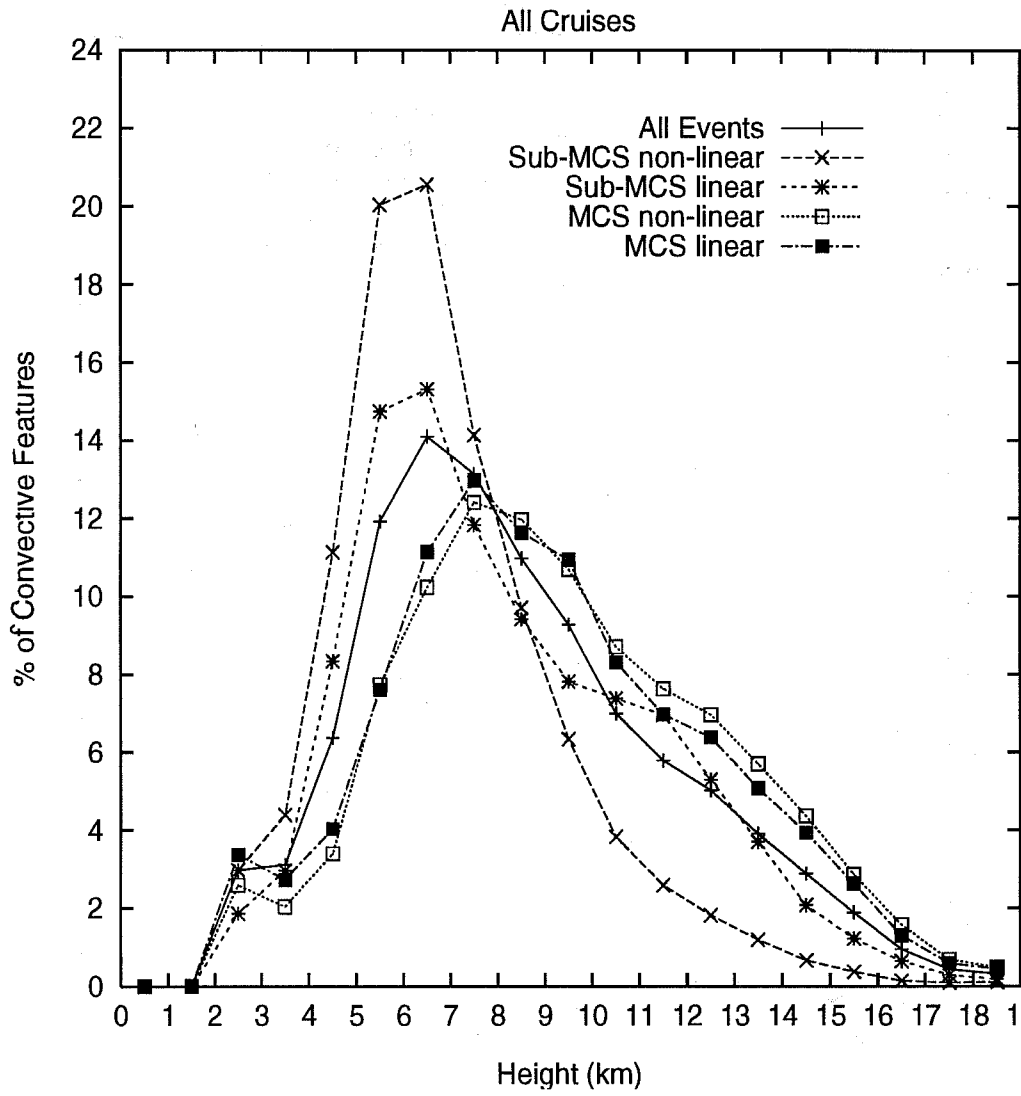

Figure 11: Histograms of the number fraction of convective features occurring in 1 km convective feature height bins, for each event type and for all events combined. From Rickenbach and Rutledge (1996a).

congestus and/or cause enhanced detrainment near this level. If cloud growth is restricted to the 0°C level and just above, it limits the role freezing can play in promoting growth to yet higher levels.

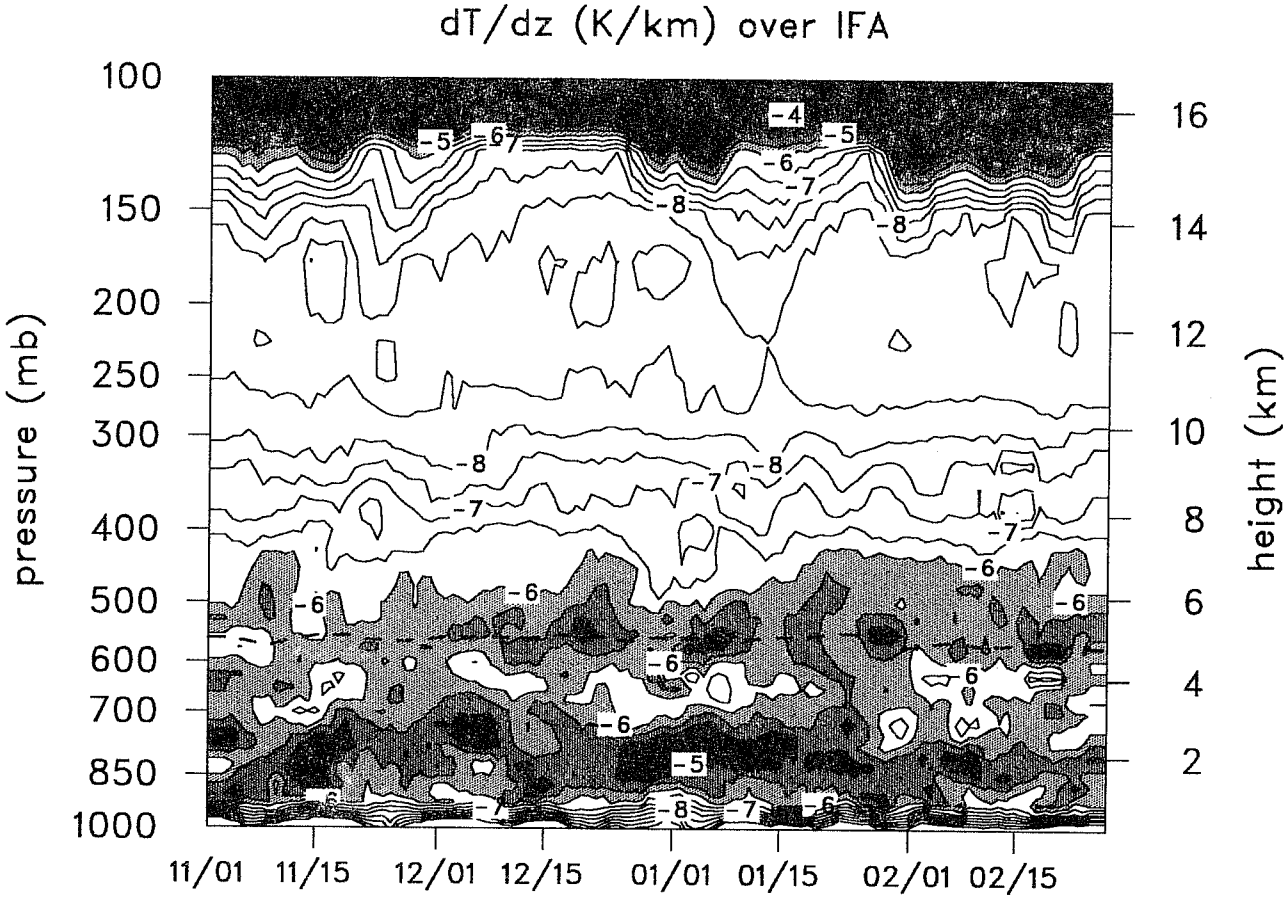

Figure 12: Time series from 1 November 1992 to 28 February 1993 of temperature lapse rate computed by averaging 25-mb gridded data (1° horizontal resolution) over the COARE Intensive Flux Array. Shaded contours indicate regions of greater stability with a contour interval of 1 C km^{-1}. Dashed line indicates 0°C level.

Analyses by RR96a of the dependence of convective type on environmental conditions (using the gridded sounding data set from Lin and Johnson 1996a) are shown in Figs. 13 and 14. Except for the sub-MCS linear cases (where the midtropospheric easterly shear is greater), the wind profiles are strikingly similar. The low-level flow for the sub-MCS non-linear cases is only slightly weaker. On the other hand, there is a pronounced difference in the moisture stratification between the MCS and sub-MCS cases: the sub-MCS cases exhibit dry mid-level conditions, presumably in association with the commonly occurring dry intrusions over the warm pool (Parsons et al. 1994, Numaguti et al. 1995), Yoneyama and Fujitani 1995 and Mapes and Zuidema 1996). The implication is that dry entrainment impacts the ability of convection to grow to MCS scale. However, caution must be exercised in this interpretation

since the soundings from the gridded data set may not accurately depict the true environment of convection in many cases.

5. DIURNAL CYCLE OF CONVECTION

A plot of the diurnal cycle of area covered by <208 K IR cloudiness (subdivided by cloud cluster size, 4 being the largest and 1 the smallest) during the COARE IOP is shown in Fig. 15 (Chen et al. 1996). The largest clusters have the greatest diurnal variation, a nearly 10:1 dawn-to-dusk ratio, with the smallest clusters having only a minor diurnal variation (as also found by Mapes and Houze 1993).

The nighttime maximum in rainfall from large convective systems is further supported by shipboard radar measurements. The diurnal variation in rainfall for all convective and non-convective events is shown in Fig. 16a (from Rickenbach and Rutledge 1996b, hereafter referred to at RR96b). There is indeed a nighttime maximum in both convective and non-convective components, but in addition there is a broad maximum in convective rainfall in the afternoon and early evening. This variability can be understood by examining the separate contributions from MCS and sub-MCS events. Specifically, the diurnal cycle of the non-linear events (which showed the largest diurnal signal of all MCS cases) is shown in Fig. 16b. A sharp peak in convective rain occurs near 0100 L with a broader maximum in non-convective (or stratiform) rainfall several hours later (reflecting the life cycle of convection). There is a weak afternoon maximum in convective rainfall. On the other hand, the sub-MCS non-linear events (Fig. 16c) showed a sharp bimodal structure for the convective component. RR96b have carried out a harmonic analysis of these data and shown that both the diurnal and semi-diurnal harmonics explain a large part of the convective variance. However, almost none of the non-convective variance (non-convective rain in the sub-MCS category was principally from collapsing convective cells) was in the diurnal harmonic. These results suggest that the semi-diurnal rain variation involves the modulation of the ice phase of deep convection, whereas the diurnal variation involves the warm-rain process. This diurnal variation for the sub-MCS events is likely a consequence of the large afternoon peak in SST (~2-3°C diurnal cycle amplitude) that often occurs on clear (associated with drier conditions aloft for sub-MCS cases, Fig. 14) and light-wind days (Weller and Anderson 1996).

The nighttime maximum in MCS convective events are consistent with the cloud-environment radiative forcing proposed by Gray and Jacobsen (1977). An equally plausible argument for an afternoon minimum in convection, though, invokes increasing stability of the upper troposphere from shortwave heating during the day (Randall et al. 1991). However, it is noted by Chen and Houze (1996) that surface boundary layer processes must also be considered to explain the full diurnal cycle since large MCSs frequently develop from convection that responds to afternoon heating of the upper ocean.

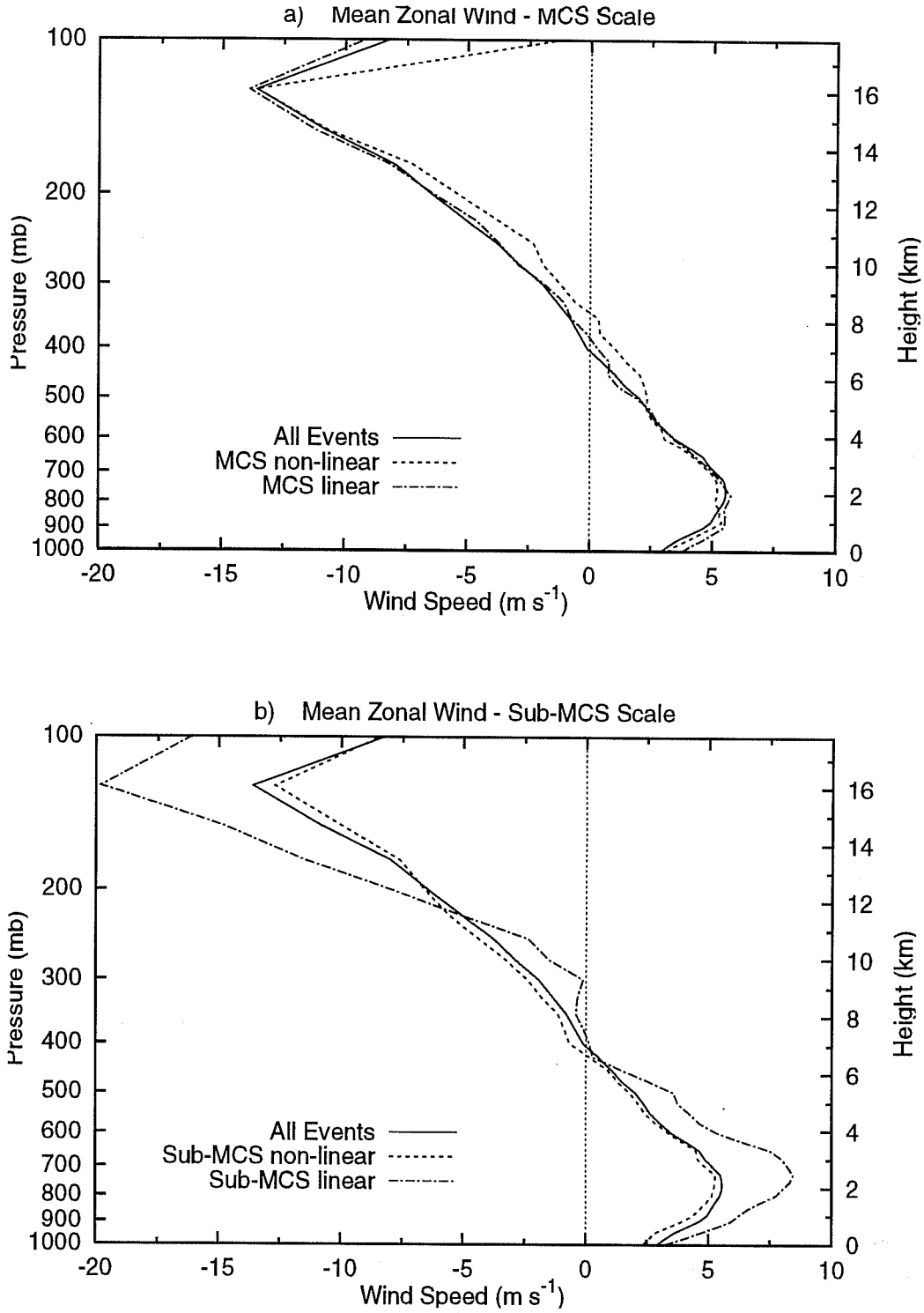

Figure 13: Mean vertical profile of zonal wind (m s^{-1}) for a) MCS scale events, and b) sub-MCS scale events. The three-cruise mean profile is also shown. Zonal wind was interpolated from the six closest sounding sites to the nominal position of the R/V *Vickers*. From Rickenbach and Rutledge (1996a).

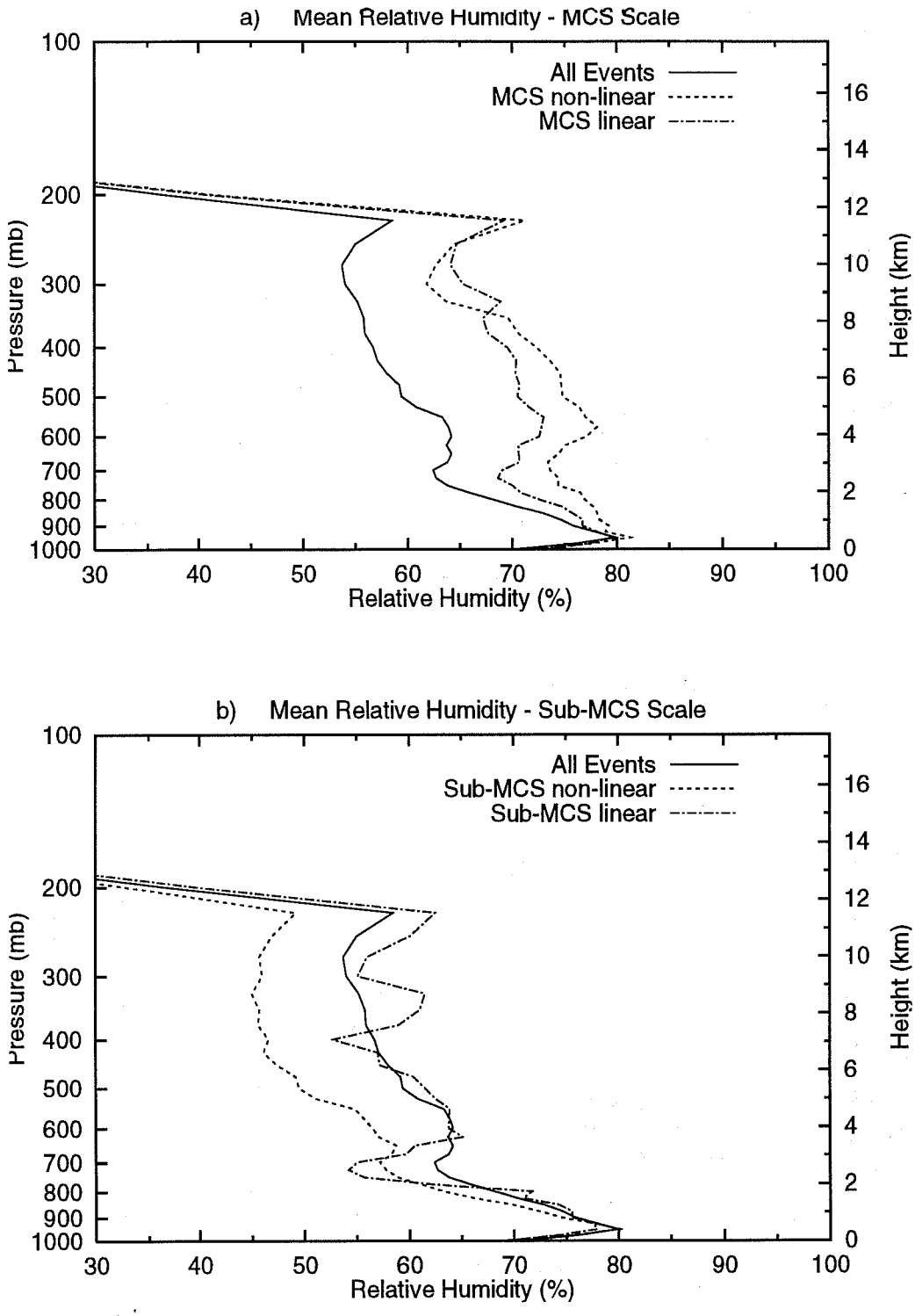

Figure 14: As in Figure 13 but for relative humidity (%) for a) MCS scale events, and b) sub-MCS scale events. The sharp decrease in relative humidity above 200 mb is due to ice covering the water vapor sensor. From Rickenbach and Rutledge (1996a).

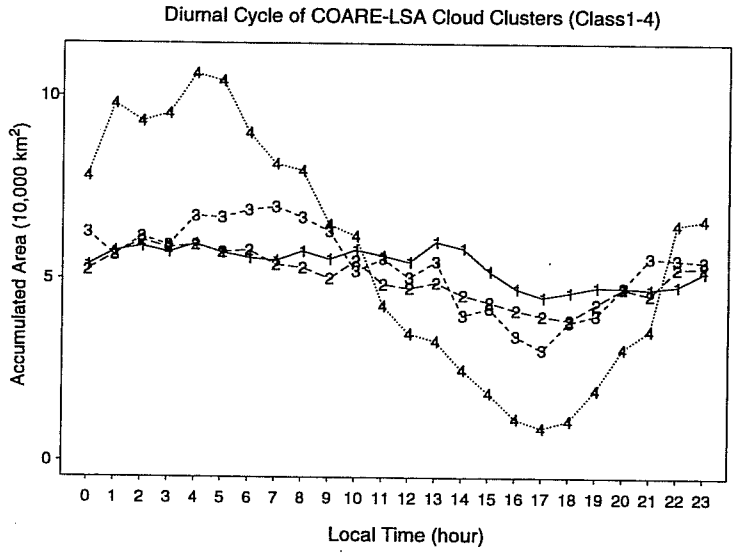

Figure 15: Diurnal cycle of the accumulated cloudy area covered by the 208 K cloud clusters over the domain of 10°N - 10°S, 152°E - 180° for each of the four size classes. From Chen et al. (1996).

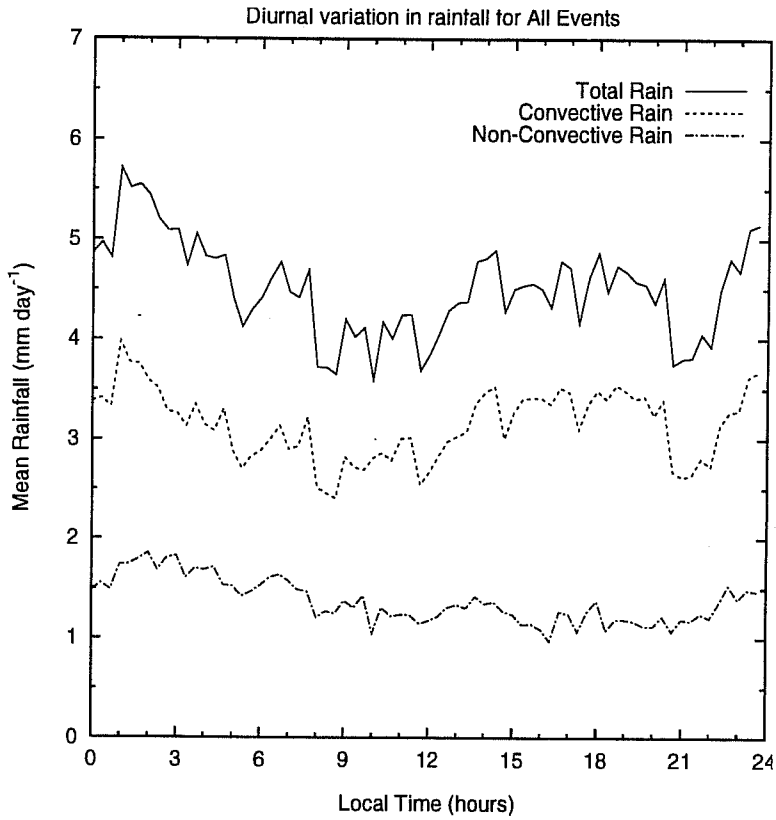

Figure 16: a) Diurnal composite of total rain, convective rain, and non-convective rain (mm day^{-1}) for all event types combined. From Rickenbach and Rutledge (1996a).

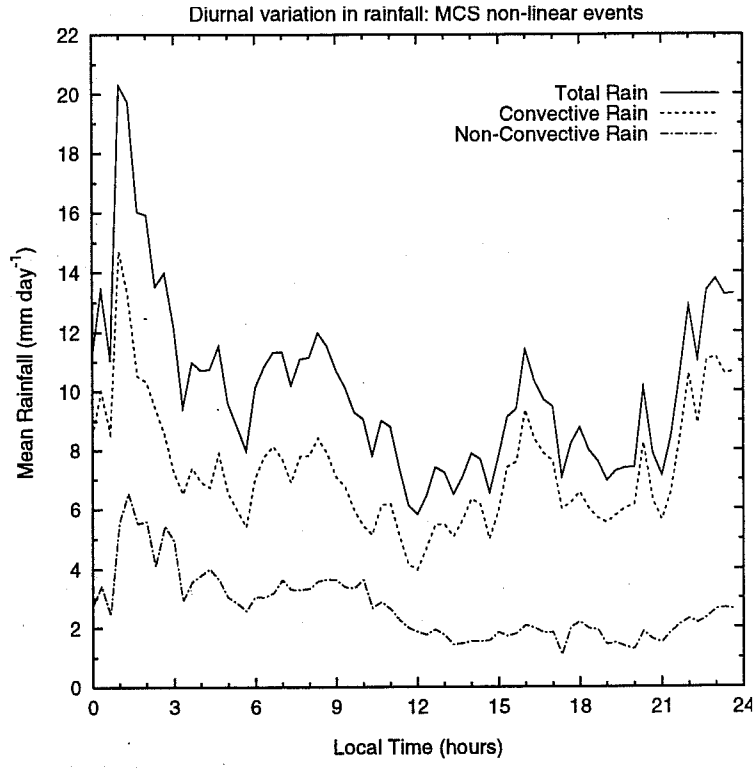

Figure 16: b) As in Figure 16a but for MCS scale non-linear events.

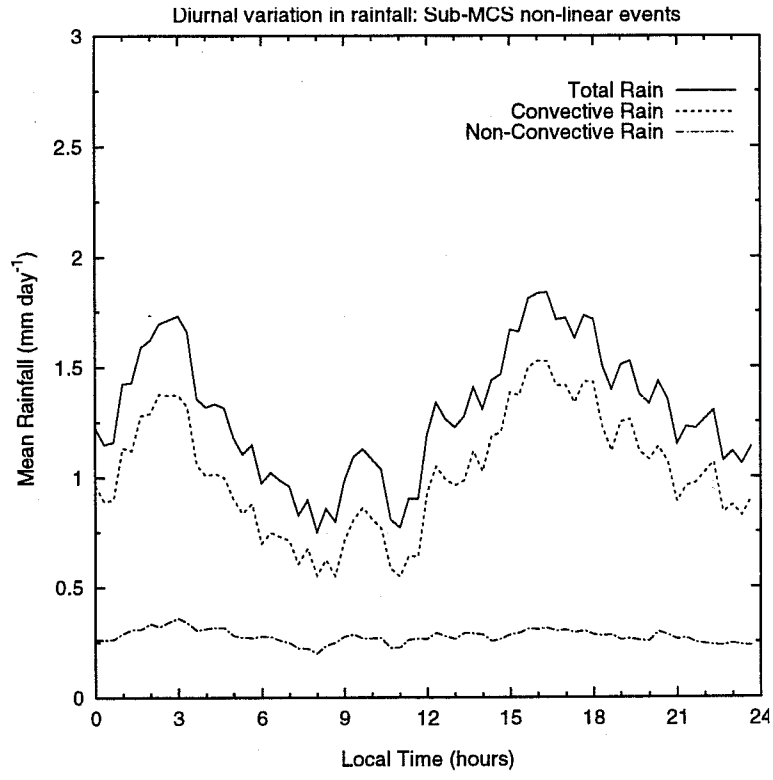

Figure 16: c) As in Figure 16a but for sub-MCS scale non-linear events.

6. COUPLING WITH THE UPPER OCEAN

Deep convection over the western Pacific warm pool significantly affects the upper ocean structure, which in turn feeds back to affect deep convection. The coupling is illustrated schematically in Fig. 17 (from Webster 1994). Webster notes that after the main westerly wind burst period (late December to early January), the SST returns to pre-burst values in about 10 days. During the relatively light-wind conditions following the burst, a shallow near-surface warm ocean layer overlaying the cooled subsurface layer is produced by solar heating, but it is too shallow to affect the anomalous heat content in the upper 200 m of the ocean significantly. Subsequent wind events mix down this warm layer and eventually establish the heat content of the upper ocean but over a much longer period. Part of the heat loss during the westerly burst period is due to evaporation and enhanced turbulent mixing in the upper ocean, but some may also be a consequence of a dynamic response of the upper ocean to the wind bursts in the form of Kelvin waves. Of course, once the SST returns to high levels following the burst, boundary-layer θ_e and instability increase to the point where deep convection and precipitation again become prevalent (Fig. 4).

7. CONCLUSIONS

Some aspects of convection over the western Pacific warm pool during TOGA COARE have been reviewed. The review is clearly incomplete, but mention has been made of findings principally from sounding and ship-radar data concerning the variability of convection on long and short-term time scales. Results suggest that the organization of convection into large MCS systems over the warm pool is more dependent on the moisture stratification than the wind shear. A clear diurnal signal in convection is present but it is complex: MCS events peak at night, whereas sub-MCS systems peak both in the afternoon and at night. The upper ocean is affected significantly by westerly wind bursts, precipitation and solar radiation and in turn feeds back to modulate deep convection.

6. ACKNOWLEDGMENTS

This research has been supported by the National Oceanic and Atmospheric Administration under Grant NA37RJ0202. Discussions with and the assistance of Xin Lin, Tom Rickenbach, Paul Ciesielski, Steve Rutledge, Wayne Schubert, Jim Bresch and Pat Haertel are greatly appreciated.

7. REFERENCES

Chen, S.S., R.A. Houze, Jr., and B.E. Mapes, 1996: Multiscale variability of deep convection in relation to large-scale circulation during TOGA-COARE. *J. Atmos. Sci.*, **53**, 1380-1409.

Fairall, C.W., E.F. Bradley, D.P. Rogers, J.B. Edson and G.S. Young, 1996: Bulk parameterization of air-sea fluxes for TOGA COARE. *J. Geophys. Res.* **101**, No. C2, 3747-3764.

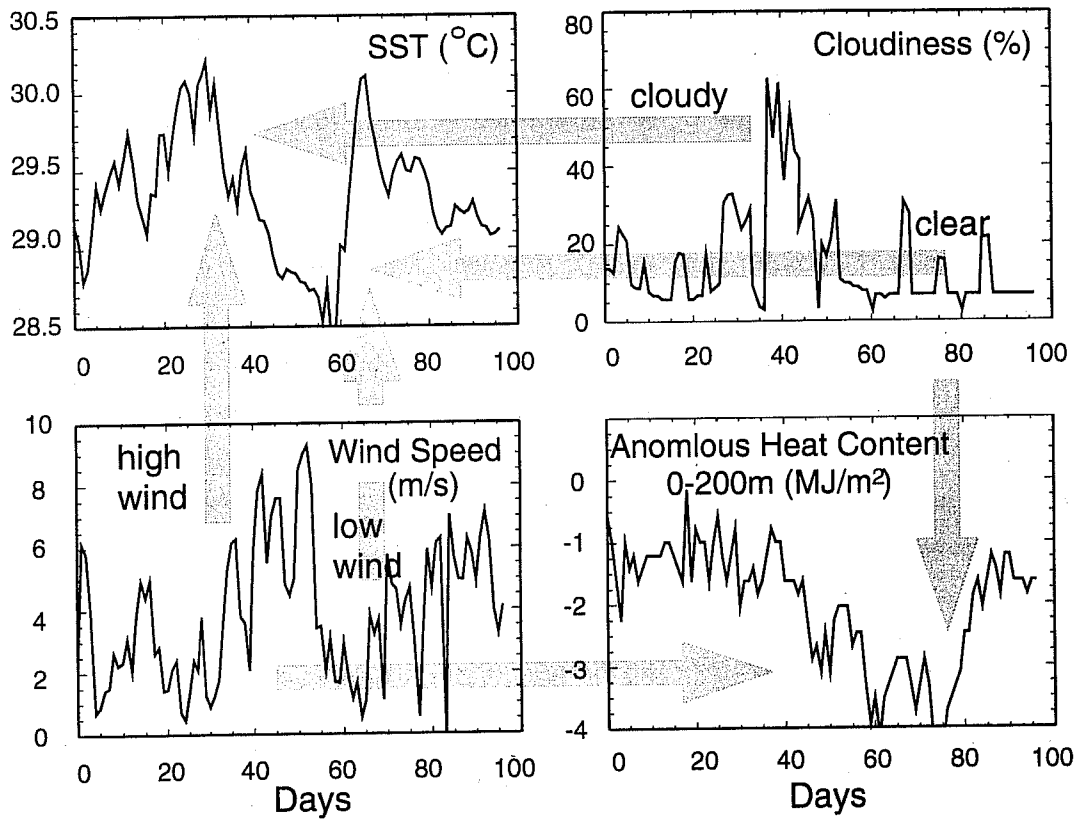

Figure 17: Example of ocean-atmosphere interaction during the western Pacific Tropical Ocean-Global Atmosphere Coupled Ocean-Atmosphere Response Experiment (TOGA COARE) held in the western Pacific ocean, November 1992 to February 1993. Shown are the evolution of SST (in degrees Celsius; top left), wind speed (in meters per second; bottom left), a measure of cloudiness using outgoing longwave radiation (OLR < 235 K; top right), and the 0-200 m heat content (megajoules per square meter; lower right). The large arrows indicate the roles of wind (through deep mixing and evaporation) and insolation (heating) play in modifying the SST and the subsurface ocean structure. From Webster (1994).

Gray, W.M., and R.W. Jacobsen, 1977: Diurnal variation of oceanic deep convection. *Mon. Wea. Rev.*, **105**, 1171-1188.

Gutzler, D.S., G.N. Kiladis, G.A. Meehl, K.M. Weickmann, and M. Wheeler, 1994: The global climate of December 1992-February 1993. Part II: Large-scale variability across the tropical western Pacific during TOGA COARE. *J. Climate*, **7**, 1606-1622.

Johnson, R.H., 1984: Partitioning tropical heat and moisture budgets into cumulus and mesoscale components: Implications for cumulus parameterization. *Mon. Wea. Rev.*, **112**, 1590-1601.

Johnson, R.H., and X. Lin, 1996: Westerly wind bursts and the distribution of atmospheric heating and moistening over the western Pacific warm pool. *J. Atmos. Sci.*, (submitted)

Johnson, R.H., P.E. Ciesielski, and K.A. Hart, 1996: Tropical inversions near the 0°C level. *J. Atmos. Sci.*, **53**, 1838-1855.

Kiladis, G.N., H. von Storch, and H. van Loon, 1989: Origin of the South Pacific convergence zone. *J. Climate*, **2**, 1185-1195.

Lin, X., and R.H. Johnson, 1996a: Kinematic and thermodynamic characteristics of the flow over the western Pacific warm pool during TOGA COARE. *J. Atmos. Sci.*, **53**, 695-715.

Lin, X., and R.H. Johnson, 1996b: Heating, moistening and rainfall over the western Pacific warm pool during TOGA COARE. *J. Atmos. Sci.*, (in press)

Mapes, B.E., and R.A. Houze, Jr., 1993: Cloud clusters and superclusters over the oceanic warm pool. *Mon. Wea. Rev.*, **121**, 1398-1415.

Mapes, B.E., and P. Zuidema, 1996: Radiative-dynamical consequences of dry tongues in the tropical atmosphere. *J. Atmos. Sci.*, **53**, 620-638.

Nakazawa, T., 1995: Intraseasonal oscillations during the TOGA-COARE IOP. *J. Meteor. Soc. Japan*, **73**, 305-319.

Nitta, T., and S. Esbensen, 1974: Heat and moisture budget analyses using BOMEX data. *Mon. Wea. Rev.*, **102**, 17-28.

Numaguti, A., R. Oki, K. Nakamura, K. Tsuboki, N. Misawa, T. Asai, and Y.-M. Kodama, 1995: 4–5-day-period variations and low-level dry air observed in the equatorial western Pacific during the TOGA-COARE IOP. *J. Meteor. Soc. Japan*, **73**, 267-290.

Parsons, D., W. Dabberdt, H. Cole, T. Hock, C. Martin, A.-L. Barrett, E. Miller, M. Spowart, M. Howard, W. Ecklund, D. Carter, K. Gage, and J. Wilson, 1994: The Integrated Sounding System: Description and preliminary observations from TOGA COARE. *Bull. Amer. Meteor. Soc.*, **75**, 553-567.

Randall, D. A., Harshvardan and D. A. Dazlich, 1991: Diurnal variability of the hydrological cycle in a general circulation model. *J. Atmos. Sci.*, **48**, 40-62.

Rickenbach, T.M., and S.A. Rutledge, 1996a: Convection in TOGA COARE: Horizontal scale, morphology and rainfall production. *J. Atmos. Sci.*, (submitted)

Rickenbach, T.M., and S.A. Rutledge, 1996b: The diurnal variation of tropical oceanic rainfall: Dependence on convective organization. *J. Atmos. Sci.*, (submitted)

Webster, P.J., 1994: The role of hydrological processes in ocean-atmosphere interactions. *Rev. Geophys.*, **32**, 427-476.

Webster, P.J., and R. Lukas, 1992: TOGA COARE: The Coupled Ocean-Atmosphere Response Experiment. *Bull. Amer. Meteor. Soc.*, **73**, 1377-1416.

Yanai, M. S. Esbensen, and J.H. Chu, 1973: Determination of bulk properties of tropical cloud clusters from large-scale heat and moisture budgets. *J. Atmos. Sci.*, **30**, 611-627.

Yoneyama, K., and T. Fujitani, 1995: The behavior of dry westerly air associated with convection observed during TOGA-COARE R/V Natsushima cruise. *J. Meteor. Soc. Japan*, **73**, 291-304.